Research Article

Humaira Yasmin*, Laila A. AL-Essa, Showkat Ahmad Lone, Hussam Alrabaiah, Zehba Raizah, and Anwar Saeed*

Magnetohydrodynamic water-based hybrid nanofluid flow comprising diamond and copper nanoparticles on a stretching sheet with slips constraints

https://doi.org/10.1515/phys-2024-0007
received December 22, 2023; accepted February 10, 2024

Abstract: Hybrid nanofluid problems are used for augmentation of thermal transportation in various industrial applications. Therefore, the present problem is studied for the heat and mass transportation features of hybrid nanofluid caused by extending surface along with porous media. In this investigation, the authors have emphasized to analyze hybrid nanofluid flow containing diamond and copper nanoparticles on an extending surface. Furthermore, the velocity, temperature, and concentration slip constraints are adopted to examine the flow of fluid. Heat source, chemical reactivity, thermal radiation, Brownian motion and effects are taken into consideration. Nonlinear modeled equations are converted into dimensionless through similarity variables. By adopting the homotopy analysis method, the resulting equations are simulated analytically. The impacts of various emerging factors on the flow profiles (*i.e.*, velocities, temperature, concentration, skin frictions, local Nusselt number, and Sherwood number) are shown using Figures and Tables. The major key findings reveal that the hybrid nanofluid temperature is higher but the concentration is lower for a Brownian diffusivity parameter. Moreover, increment role of heat transport is achieved due to the increment in radiation factor, thermophoresis, Brownian motion factors, and Eckert number. It has also been observed that velocity in x-direction converges in the region $-0.8 \le \hbar_f \le 0.5$, in y-direction velocity is convergent in the zone $-0.6 \le \hbar_g \le 0.35$, while temperature converges in the region $-0.6 \le \hbar_\theta \le 0.4$ and concentration converges in the region $-0.5 \le \hbar_\varphi \le 0.4$.

Keywords: hybrid nanofluid flow, MHD, porous media, thermal radiation, heat source, stretching surface, slip conditions

Nomenclature

B_0	strength of magnetic field
C	concentration
C_p	specific heat
D_B	coefficient of Brownian diffusion
D_T	thermophoretic coefficient
E	activation energy factor
E_a	coefficient of activation energy
Ec	Eckert number
K	porosity factor
K^*	coefficient of porous media
K_r	chemical reaction
k	thermal conductivity
k^*	mean absorption coefficient
k_r	coefficient of chemical reaction
m	power index
M	magnetic factor
Nb	Brownian motion factor

*** Corresponding author: Humaira Yasmin,** Department of Basic Sciences, General Administration of Preparatory Year, King Faisal University, P.O. Box 400, Al Ahsa, 31982, Saudi Arabia; Department of Mathematics and Statistics, College of Science, King Faisal University, P.O. Box 400, Al Ahsa, 31982, Saudi Arabia, e-mail: hhassain@kfu.edu.sa
*** Corresponding author: Anwar Saeed,** Department of Mathematics, Abdul Wali Khan University, Mardan, 23200, Khyber Pakhtunkhwa, Pakistan, e-mail: anwarsaeed769@gmail.com
Laila A. AL-Essa: Department of Mathematical Sciences, College of Science, Princess Nourah bint Abdulrahman University, P.O.Box 84428, Riyadh, 11671, Saudi Arabia
Showkat Ahmad Lone: Department of Basic Sciences, College of Science and Theoretical Studies, Saudi Electronic University, (Jeddah-M), Riyadh, 11673, Saudi Arabia
Hussam Alrabaiah: College of Engineering, Al Ain University, Al Ain, United Arab Emirates; Mathematics Department, Tafila Technical University, Tafila, Jordan
Zehba Raizah: Department of Mathematics, College of Science, King Khalid University, Abha, Saudi Arabia

Nt	thermophoresis factor
Pr	Prandtl number
P_1	first nanoparticle
P_2	second nanoparticle
Q	heat source factor
Q_0	heat source coefficient
q_r	radiative heat flux
Sc	Schmidt number
T	temperature
u, v, w	velocity components
x, y, z	coordinates
μ	dynamic viscosity
ρ	density
σ_1	primary velocity slip constant
σ_2	secondary velocity slip constant
σ_3	temperature slip constant
σ_4	concentration slip constant
σ^*	Stefan–Boltzmann constant
ϕ_1	volume fraction of first nanoparticle
ϕ_2	volume fraction of second nanoparticle
β	temperature difference factor
δ	ratio factor
α_1	primary velocity slip factor
α_2	secondary velocity slip factor
α_3	temperature slip factor
α_4	concentration slip factor

1 Introduction

In the realm of advanced fluid dynamics and heat transfer research, the analysis of nanofluids has arose as a promising frontier with profound implications for various engineering applications. Magnetohydrodynamic (MHD) nanofluids, characterized by the synergistic coupling of magnetic field effects and nanoparticle dispersion within a fluid medium, have gathered substantial attention due to their potential to enhance thermal performance and control fluid flow behavior. This study delves into the complex dynamics of a MHD water-based hybrid nanofluid, composed of diamond and copper nanoparticles, as it flows over a stretching sheet; a scenario often encountered in industrial processes and engineering systems. Furthermore, the inclusion of slip boundary conditions adds an additional layer of complexity to the investigation, making this study a significant contribution to the evolving field of MHD nanofluid mechanics and its practical implications. In this context, the present work seeks to unravel the elaborated interaction of magnetic fields, nanoparticle additives, and slip effects on fluid flow and heat transfer characteristics, offering valuable insights for optimizing cooling systems, heat exchangers, and other thermal controlling applications at industrial level.

Nanofluid is a promising category of thermal transmission fluids that have been increasingly used in numerous areas, including aerospace engineering, automobile industry, and energy systems. The reason for their popularity is their unique properties that are not found in conventional fluids. Nanofluid is a mixture of a pure fluid and nanoparticles, which improves the thermal flow characteristics and thermal flow ability of fluid. Choi and Eastman [1] are the pioneers of the idea. Hashemi *et al.* [2] scrutinized thermal flow enhancement of a nanofluid flow in a conduit and observed that accumulation of nanoparticles significantly enhanced the coefficient of heat transference and improved the fluid's overall thermal performance. Habib *et al.* [3] inspected MHD nanoparticles-based fluid flow subject to microorganisms and melting effects. Chu *et al.* [4] debated on the comparison for model-based study on MHD nanofluid flow amid two plates using the impact of nanoparticles shape. Eid and Nafe [5] examined the variation in thermal conductance and creation of heat for nanofluid MHD flow past a permeable sheet using slip constraints and found that growth in nanoparticles volume has augmented the thermal profiles while the velocity panels have weakened accordingly. Rajput *et al.* [6] explored numerically the nanoparticle's radius impact on water-based nanofluid consisting of copper nanoparticles across an extending permeable surface with slip condition. Sarfraz and Khan [7] used the impacts of nanoparticles and dual diffusions on fluid flow induced by movable plate and observed that fluid velocity has declined with escalation in magnetic factor. Dawar *et al.* [8] examined non-homogenous MHD nanofluid flow model to simulate rotary thin inclined layer and concluded that augmentation in thermophoresis factor has weakened the concentration panels while thermal characteristics have augmented. Pasha *et al.* [9] studied statistically the entropy creation for nanofluid flow on permeable stretched sheet with impact of different shapes of nanoparticles and have deduced that the entropy of system has expanded for growth in nanoparticles concentration, Biot number, and radiation factor.

Hybrid nanofluids are mixing of multiple nanoparticles in pure fluid, which engrossed the attention of researchers. Such fluids have unique properties that are not present in single-nanoparticle nanofluids. For instance, hybrid nanofluids can have enhanced thermal, electrical conductivities, and heat transfer properties, making them useful in numerous applications like coolant of electric devices, nuclear reactor, and thermal exchangers. The behavior of hybrid nanofluids flow is affected by various features, including the size, shape, and concentration of nanoparticles, along with type and flow rate of pure fluid. Ojjela [10] investigated numerically the time-

based silica–alumina hybrid nanofluid flow on an extended sheet using magnetic effects and has deduced that thermal distribution has augmented whereas velocity panels decreased with the increase in the concentration of nanoparticles. Sarfraz *et al.* [11] inspected thermal transference for radiative trihybrid nanofluid flow on an elongating surface and proved that shape of nanoparticles impacted the transportation of heat. Salahuddin *et al.* [12] debated on three-dimensional hybrid nanofluid flow at s stagnant point of wavy, heated, and stretched cylinder and observed that velocity panels have escalated at the beginning and end of the cylinder with the increase in nanoparticles but at the middle of the cylinder, the flow has declined. Zhang *et al.* [13] scrutinized nanoparticles flow near the elastic surface by employing nickel and tantalum nanoparticles with the effect of magnetic field. Sarfraz *et al.* [14] inspected stagnant point flow for hybrid nanofluid on spiraling and elongating sheet and noticed that fluid transportation of heat has augmented with the increase in the surface porosity. Alrabaiah *et al.* [15] deliberated on impact of gyrotactic microorganisms on hybrid nanofluid flow in the gap of cone and disk. Ouni *et al.* [16] debated on the thermal solar features for hybrid nanofluid flow in a solar collector by mixing gold and copper nanoparticles in engine oil. Barathi *et al.* [17] studied computationally the thermal transference for trihybrid EMHD nanofluid flow on a permeable surface. Pandey *et al.* [18] discussed the effect of iron oxide nanoparticles on the unsteady hybrid nanoliquid flow across a flat surface. Ahmed *et al.* [19] simulated computationally the hybrid nanofluid flow thorough annular sector of duct. Singh *et al.* [20] discussed thermal transference and impacts of thermally radiated trihybrid nanofluid flow on an elongating surface. Some valuable results are recently presented in previous studies [21–23].

The study of fluid's behavior that is conducted electrically with impact of magnetic effects is called MHD. Recently, investigation of MHD fluid flow has gained immense consideration for its application like plasma propulsion, metallurgy, materials processing *etc*. In this literature review, we discuss recent advances in the field of MHD fluid flow. One of the fundamental problems in MHD fluid flow is the study of the permanency of the flow. The stability of MHD flow is an essential aspect of many industrial applications. Dey *et al.* [24] debated on the effects of zero mass flux and slip condition on the MHD nanoliquid flow across a plate surface. Goud Bejawada *et al.* [25] discussed radiative influences on MHD fluid flow on a sheet using the impact of a chemical reaction. Vishalakshi *et al.* [26] examined the MHD fluid flow on a shrinking and elongating permeable sheet subject to mass transportation and slip constraints and noted that the thermal and velocity distributions have augmented with the increase in the concentration of nanoparticles and radiative factor. Upreti *et al.* [27] considered the effects of radiations and heat sink/source on nanofluid flow over a permeable surface. Sharma *et al.* [28] inspected the convective MHD fluid flow on a gyrating disk and deduced velocity of fluid has opposed while thermal distribution has supported with progression in magnetic parameter. Raghunath *et al.* [29] studied the MHD fluid flow on a permeable surface using chemically reactive and radiation impacts and concluded that velocity panel was found to increase with the increase in the Soret and permeability factors while it weakened with augmentation in magnetic and inclined parameters. Many similar effects can be studied in previous literature [30–34].

Fluid flow over porous surfaces is a fundamental and ubiquitous phenomenon in many engineering and natural systems, such as ground water flow, geothermal energy extraction, oil reservoirs *etc*. Porous media, which are characterized by their porosity, permeability, and tortuosity, play a critical role in controlling fluid flow behavior. Porous media is commonly found in natural systems such as aquifers, soils, and rocks, and in engineered systems such as geothermal energy systems, catalytic reactors, and biomedical devices. When fluid flows over a porous surface, it can penetrate into the pores of the surface and interact with the material inside. Akbar Qureshi *et al.* [35] evaluated the impression of MHD flow of fluid on a permeable and orthogonal surface subject to effects of injection and small walled carbon nano tubes (SWCNTs) and inferred that the thermal panels enlarged with the increase in the porosity of the surface. Verma *et al.* [36] discussed the stability and comparative study of graphene oxide/water and graphene/water-based nanofluid flows across a permeable stretching surface. Raza *et al.* [37] scrutinized the hybrid nanoparticles flow on a porous sheet using the impacts of chemically reactive activated energy and magnetic field and detected that velocity panels have weakened for intensification in concentration of nanoparticles while thermal characteristics have increased. Krishna and Chamkha [38] inspected chemically reactive and Hall effects with slip constraints on MHD rotary flow over a porous infinite vertical sheet and have assumed velocity panels have diminished while thermal panels have increased with the increase in the porosity factor. Megahed and Abbas [39] discussed fluid flow on porous surface and highlighted that thermal panels have improved with progress in permeability factor while concentration characteristics have declined in this phenomenon. Pandey *et al.* [40] inspected free convective MHD flow of hybrid nanoparticles on a permeable surface subject to various slip constraints and have proved that velocity and concentration have weakened with expansion in natural convective factor.

Hybrid nanofluid has remarkable applications, while flowing across a stretching permeable surface, such as oil recovery, thermal transportation, automobiles, electronics equipment's, vehicle engines, drug delivery, and biomedical fields. Therefore, the present problem is modeled based on the above applications of hybrid nanofluid flow, to evaluate the thermal characteristics of nanofluid consisting of diamond and copper nanoparticles across an extending surface. Furthermore, chemical reactivity, heat source, and thermal radiation effects along with activation energy features are taken into consideration. Thus, in this analysis, the authors are interested to answer the following research questions:

- How do the slip parameter, ratio parameter, porosity parameter, and magnetic parameter affect the primary and secondary velocities?
- How do the Eckert number, Brownian motion factor, heat generation factor, and thermal radiation factor affect the flow temperature?
- How do the thermophoresis factor, activation energy factor, Brownian motion factor, and Schmidt number affect the flow concentration?
- How do the embedded factors affect the skin frictions, local Nusselt number, and Sherwood number?

To answer the above questions, the present analysis is composed of subsequent sections. Section 2 presents the mathematical formulation fluid flow, which consists of diamond and copper nanoparticles. The solution of the transformed ODEs is tackled with the semi-analytical method called homotopy analysis method (HAM), which is described in Section 3. The convergence of the applied technique is shown in Section 4. Section 5 has two sub-sections. Sub-Section 5.1 presents the obtained results, and sub-Section 5.2 presents the physical discussion of the obtained results. The final concluding remarks are presented in Section 6.

2 Formulation of problem

Assume 3D flow of hybrid nanofluid (composed of diamond and copper nanoparticles while water is considered as pure fluid), over an elongating sheet with porous media. The surface stretches with velocity $u_w(x) = ax$ along x-direction and along y-direction with velocity $v_w(y) = by$, where a and b are fixed constants. The flow is considered to be magnetically influenced by applying the strength of magnetic field B_0 in a perpendicular direction (z-axis). In the context of porous medium flow, when viscous effects predominate and the flow is characterized by low Reynolds numbers, Darcy's law is employed. The geometrical view of the considered stretching surface is shown in Figure 1. The concentration, velocity, and thermal slip constraints are adopted in this analysis. The flow of fluid is considered to be affected by various flow conditions. With above assumptions, the main equations are [41,42]:

$$\frac{\partial u}{\partial x} + \frac{\partial v}{\partial y} + \frac{\partial w}{\partial z} = 0, \tag{1}$$

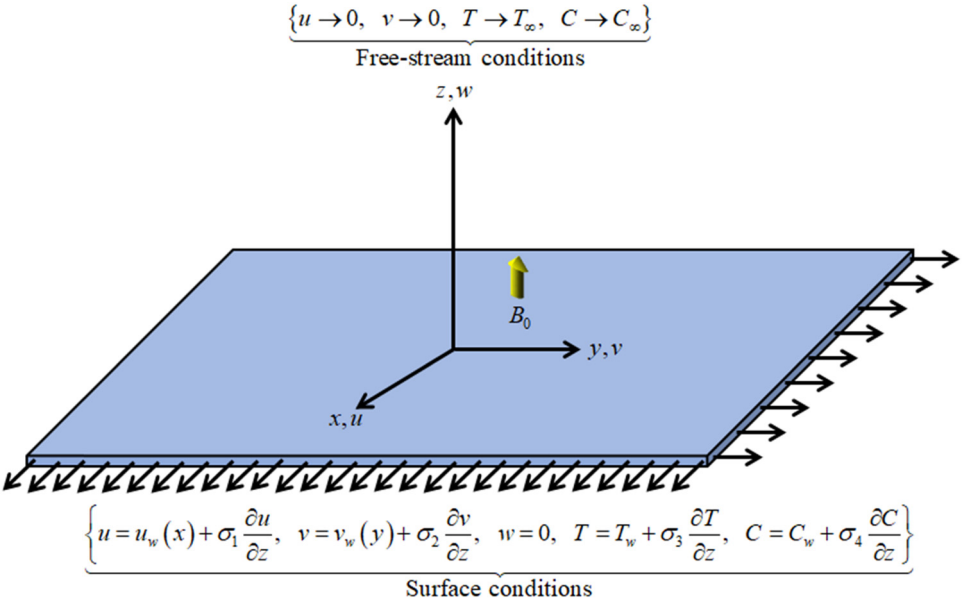

Figure 1: Geometrical view of the flow problem.

$$u\frac{\partial u}{\partial x} + v\frac{\partial u}{\partial y} + w\frac{\partial u}{\partial z} = \frac{\mu_{\text{hnf}}}{\rho_{\text{hnf}}}\frac{\partial^2 u}{\partial z^2} - \left(\frac{\sigma_{\text{hnf}}}{\rho_{\text{hnf}}}B_0^2 + \frac{\mu_{\text{hnf}}}{\rho_{\text{hnf}}}\frac{1}{K^*}\right)u, \tag{2}$$

$$u\frac{\partial v}{\partial x} + w\frac{\partial v}{\partial z} + v\frac{\partial v}{\partial y} = \frac{\mu_{\text{hnf}}}{\rho_{\text{hnf}}}\frac{\partial^2 v}{\partial z^2} - \left(\frac{\sigma_{\text{hnf}}}{\rho_{\text{hnf}}}B_0^2 + \frac{\mu_{\text{hnf}}}{\rho_{\text{hnf}}}\frac{1}{K^*}\right)v, \tag{3}$$

$$\begin{aligned} u\frac{\partial T}{\partial x} + v\frac{\partial T}{\partial y} + w\frac{\partial T}{\partial z} &= \frac{k_{\text{hnf}}}{(\rho C_{\text{p}})_{\text{hnf}}}\frac{\partial^2 T}{\partial z^2} - \frac{1}{(\rho C_{\text{p}})_{\text{hnf}}}\frac{\partial q_{\text{r}}}{\partial z} \\ &\quad - \frac{1}{(\rho C_{\text{p}})_{\text{hnf}}}Q_0(T - T_\infty) \\ &\quad + \frac{\mu_{\text{hnf}}}{(\rho C_{\text{p}})_{\text{hnf}}}\left(\left(\frac{\partial u}{\partial z}\right)^2 + \left(\frac{\partial v}{\partial z}\right)^2\right) \\ &\quad + \frac{(\rho C_{\text{p}})_{\text{np}}}{(\rho C_{\text{p}})_{\text{hnf}}}\left(\frac{D_{\text{B}}}{\delta_{\text{C}}}\frac{\partial T}{\partial z}\frac{\partial C}{\partial z} + \frac{D_{\text{T}}}{T_\infty}\left(\frac{\partial T}{\partial z}\right)^2\right), \end{aligned} \tag{4}$$

Following Cao *et al.* [43] and Song *et al.* [44], we have

$$u\frac{\partial C}{\partial x} + v\frac{\partial C}{\partial y} + w\frac{\partial C}{\partial z} = D_{\text{B}}\frac{\partial^2 C}{\partial z^2} + \frac{\delta_{\text{C}}D_{\text{T}}}{T_\infty}\frac{\partial^2 T}{\partial z^2} - k_{\text{r}}^2(C - C_\infty)\left(\frac{T}{T_\infty}\right)^m e^{\left(-\frac{E_{\text{a}}}{k_{\text{B}}T}\right)}. \tag{5}$$

The boundary conditions are defined as follows:

$$\left.\begin{aligned} &u = u_{\text{w}}(x) + \sigma_1\frac{\partial u}{\partial z}, v = v_{\text{w}}(y) + \sigma_2\frac{\partial v}{\partial z}, w = 0, \\ &T = T_{\text{w}} + \sigma_3\frac{\partial T}{\partial z}, C = C_{\text{w}} + \sigma_4\frac{\partial C}{\partial z} \text{ at } z = 0, \\ &u \to 0, v \to 0, T \to T_\infty, C \to C_\infty \text{ as } z \to \infty. \end{aligned}\right\} \tag{6}$$

The value of q_{r} is given as

$$q_{\text{r}} = -\frac{4\sigma^*}{3k^*}\frac{\partial T^4}{\partial z} = -\frac{16\sigma^*}{3k^*}\frac{\partial^2 T}{\partial z^2}. \tag{7}$$

Thus, Eq. (5) can be written as

$$\begin{aligned} u\frac{\partial T}{\partial x} + v\frac{\partial T}{\partial y} + w\frac{\partial T}{\partial z} &= \frac{k_{\text{hnf}}}{(\rho C_{\text{p}})_{\text{hnf}}}\frac{\partial^2 T}{\partial z^2} + \frac{1}{(\rho C_{\text{p}})_{\text{hnf}}}\frac{16\sigma^*}{3k^*}\frac{\partial^2 T}{\partial z^2} \\ &\quad - \frac{1}{(\rho C_{\text{p}})_{\text{hnf}}}Q_0(T - T_\infty) + \frac{\mu_{\text{hnf}}}{(\rho C_{\text{p}})_{\text{hnf}}}\left(\left(\frac{\partial v}{\partial z}\right)^2 + \left(\frac{\partial u}{\partial z}\right)^2\right) \\ &\quad + \frac{(\rho C_{\text{p}})_{\text{np}}}{(\rho C_{\text{p}})_{\text{hnf}}}\left(\frac{D_{\text{B}}}{\delta_{\text{C}}}\frac{\partial T}{\partial z}\frac{\partial C}{\partial z} + \frac{D_{\text{T}}}{T_\infty}\left(\frac{\partial T}{\partial z}\right)^2\right), \end{aligned} \tag{8}$$

The value of μ_{hnf}(dynamic viscosity) [45,46] is

$$\mu_{\text{hnf}} = \frac{\mu_{\text{f}}}{(1 - \phi_1)^{2.5}(1 - \phi_2)^{2.5}}, \tag{9}$$

where ϕ_1 and ϕ_2 are, respectively, the volume fractions of first and second nanoparticles.

The density of the hybrid nanofluid is defined as [45,46]

$$\rho_{\text{hnf}} = ((1 - \phi_2)(\rho_{\text{f}}(1 - \phi_1) + \rho_{P_1}\phi_1)) + \rho_{P_2}\phi_2, \tag{10}$$

where P_1 and P_2 are the first and second nanoparticles.

The value of $(\rho C_{\text{p}})_{\text{hnf}}$ is given by [45,46]

$$\begin{aligned} (\rho C_{\text{p}})_{\text{hnf}} &= ((1 - \phi_2)((\rho C_{\text{p}})_{\text{f}}(1 - \phi_1) + \phi_1(\rho C_{\text{p}})_{\text{P}_1})) \\ &\quad + \phi_2(\rho C_{\text{p}})_{\text{P}_2}. \end{aligned} \tag{11}$$

The value of k_{hnf} is given as [45,46]

$$k_{\text{hnf}} = \left(\frac{\frac{k_{P_1}\phi_1 + k_{P_2}\phi_2}{\phi_1 + \phi_2} + 2k_{\text{f}} + 2(k_{P_1}\phi_1 + k_{P_1}\phi_2) - 2(\phi_1 + \phi_2)k_{\text{f}}}{\frac{k_{P_1}\phi_1 + k_{P_1}\phi_2}{\phi_1 + \phi_2} + 2k_{\text{f}} - 2(k_{P_1}\phi_1 + k_{P_1}\phi_2) + (\phi_1 + \phi_2)k_{\text{f}}}\right)k_{\text{f}}. \tag{12}$$

The value of σ_{hnf} is given by [45,46]

$$\sigma_{\text{hnf}} = \left(\frac{\frac{\sigma_{P_1}\phi_1 + \sigma_{P_2}\phi_2}{\phi_1 + \phi_2} + 2\sigma_{\text{f}} + 2(\sigma_{P_1}\phi_1 + \sigma_{P_1}\phi_2) - 2(\phi_1 + \phi_2)\sigma_{\text{f}}}{\frac{\sigma_{P_1}\phi_1 + \sigma_{P_1}\phi_2}{\phi_1 + \phi_2} + 2\sigma_{\text{f}} - 2(\sigma_{P_1}\phi_1 + \sigma_{P_1}\phi_2) + (\phi_1 + \phi_2)\sigma_{\text{f}}}\right)\sigma_{\text{f}}. \tag{13}$$

The thermophysical features of nanoparticles and water are defined in Table 1.

To transform the above PDEs, variables (similarity) are defined as [41] follows:

$$\left.\begin{aligned} &u = axf'(\zeta), v = ayg'(\zeta), w = -\sqrt{av_{\text{f}}}(g(\zeta) + f(\zeta)), \\ &\varphi(\zeta) = \frac{C - C_\infty}{C_{\text{w}} - C_\infty}, \theta(\zeta) = \frac{T - T_\infty}{T_{\text{w}} - T_\infty}, \zeta = z\sqrt{\frac{a}{v_{\text{f}}}}. \end{aligned}\right\} \tag{14}$$

The use of Eq. (14) converts the system of equation to

$$\left(\frac{\mu_{\text{hnf}}/\mu_{\text{f}}}{\rho_{\text{hnf}}/\rho_{\text{f}}}\right)f'''(\zeta) + (g(\zeta) + f(\zeta))f''(\zeta) + f'^2(\zeta) - M\left(\frac{\sigma_{\text{hnf}}/\sigma_{\text{f}}}{\rho_{\text{hnf}}/\rho_{\text{f}}}\right)f'(\zeta) - K\left(\frac{\mu_{\text{hnf}}/\mu_{\text{f}}}{\rho_{\text{hnf}}/\rho_{\text{f}}}\right)f'(\zeta) = 0, \tag{15}$$

$$\left(\frac{\mu_{\text{hnf}}/\mu_{\text{f}}}{\rho_{\text{hnf}}/\rho_{\text{f}}}\right)g'''(\zeta) + (g(\zeta) + f(\zeta))g''(\zeta) + g'^2(\zeta) - \left(\frac{\sigma_{\text{hnf}}/\sigma_{\text{f}}}{\rho_{\text{hnf}}/\rho_{\text{f}}}\right)Mg'(\zeta) - \left(\frac{\mu_{\text{hnf}}/\mu_{\text{f}}}{\rho_{\text{hnf}}/\rho_{\text{f}}}\right)Kg'(\zeta) = 0, \tag{16}$$

Table 1: Thermophysical features of nanoparticles and water [45,46]

Thermodynamic properties	Base fluid	Nanoparticles	
	Water	Diamond	Copper
ρ (kg m^{-3})	997.1	3100	8933
c_p (J kg^{-1} K^{-1})	4,179	516	385
k (Wm^{-1} K^{-1})	0.613	1,000	400
σ (Sm^{-1})	0.05	34.84×10^6	5.96×10^7

$$\left(\frac{k_{\mathrm{hnf}}/k_{\mathrm{f}}}{(\rho C_{\mathrm{p}})_{\mathrm{hnf}}/(\rho C_{\mathrm{p}})_{\mathrm{f}}} + \frac{\mathrm{Rd}}{(\rho C_{\mathrm{p}})_{\mathrm{hnf}}/(\rho C_{\mathrm{p}})_{\mathrm{f}}}\right)\theta''(\zeta) + \mathrm{Pr}\theta'(\zeta)\begin{Bmatrix} f(\zeta) \\ +g(\zeta)\end{Bmatrix} + \frac{\mathrm{Pr}Q}{(\rho C_{\mathrm{p}})_{\mathrm{hnf}}/(\rho C_{\mathrm{p}})_{\mathrm{f}}}\theta(\zeta) + \mathrm{Pr}\mathrm{Ec}\left(\frac{\mu_{\mathrm{hnf}}/\mu_{\mathrm{f}}}{(\rho C_{\mathrm{p}})_{\mathrm{hnf}}/(\rho C_{\mathrm{p}})_{\mathrm{f}}}\right)(f''^2(\zeta) + g''^2(\zeta)) + \frac{\mathrm{Pr}}{(\rho C_{\mathrm{p}})_{\mathrm{hnf}}/(\rho C_{\mathrm{p}})_{\mathrm{f}}}(\mathrm{Nb}\theta'(\zeta)\varphi'(\zeta) + \mathrm{Nt}\theta'^2(\zeta)) = 0, \tag{17}$$

$$\varphi''(\zeta) + \mathrm{Sc}\varphi'(\zeta)(f(\zeta) + g(\zeta)) + \frac{\mathrm{Nt}}{\mathrm{Nb}}\theta''(\zeta) - K_{\mathrm{r}}\mathrm{Sc}\exp\left(\frac{-E}{1 + \theta(\zeta)\beta}\right)(1 + \beta\theta(\zeta))^n\varphi(\zeta) = 0, \tag{18}$$

with transformed constraints at boundary:

$$\begin{Bmatrix} f(0) = 0, f'(0) = 1 + \alpha_1 f''(0), g'(0) = \delta + \alpha_2 g''(0), \\ g(0) = 0, \theta(0) = 1 + \alpha_3\theta'(0), \varphi(0) = 1 + \alpha_4\varphi'(0), \\ f'(\infty) \to 0, g'(\infty) \to 0, \theta(\infty) \to 0, \varphi(\infty) \to 0. \end{Bmatrix} \tag{19}$$

where $M\left(=\frac{\sigma_{\mathrm{f}}B_0^2}{\rho_{\mathrm{f}}a}\right)$ is the magnetic parameter, $\mathrm{Pr}\left(=\frac{(\rho C_{\mathrm{p}})_{\mathrm{f}}\nu_{\mathrm{f}}}{k_{\mathrm{f}}}\right)$ is the Prandtl number, $\mathrm{Ec}\left(=\frac{u_{\mathrm{w}}^2}{(C_{\mathrm{p}})_{\mathrm{f}}(T_{\mathrm{w}} - T_\infty)}\right)$ is the Eckert number, $K_{\mathrm{r}}\left(=\frac{k_{\mathrm{r}}}{a}\right)$ is the chemical reaction factor, $Q\left(=\frac{Q_0}{a(\rho C_{\mathrm{p}})_{\mathrm{f}}}\right)$ is the heat source factor, $\mathrm{Nt}\left(=\frac{D_{\mathrm{T}}(T_{\mathrm{w}} - T_\infty)(\rho C_{\mathrm{p}})_{\mathrm{np}}}{\nu_{\mathrm{f}}T_\infty(\rho C_{\mathrm{p}})_{\mathrm{f}}}\right)$ is the thermophoresis factor, $\mathrm{Nb}\left(=\frac{(C_{\mathrm{w}} - C_\infty)D_{\mathrm{B}}(\rho C_{\mathrm{p}})_{\mathrm{np}}}{\nu_{\mathrm{f}}\delta_{\mathrm{C}}(\rho C_{\mathrm{p}})_{\mathrm{f}}}\right)$ is the Brownian motion factor, $\mathrm{Sc}\left(=\frac{\nu_{\mathrm{f}}}{D_{\mathrm{B}}}\right)$ is the Schmidt number, $\beta\left(=\frac{T_{\mathrm{w}} - T_\infty}{T_\infty}\right)$ is the temperature difference factor, $E\left(=\frac{E_{\mathrm{a}}}{T_\infty k_{\mathrm{B}}}\right)$ is the factor of activation energy, $K\left(=\frac{\mu_{\mathrm{f}}}{aK^*\rho_{\mathrm{f}}}\right)$ is the porosity factor, $\delta\left(=\frac{b}{a}\right)$ is the ratio factor, $\alpha_1\left(=\sigma_1\sqrt{\frac{a}{\nu_{\mathrm{f}}}}\right)$ is the primary velocity slip factor, $\alpha_2\left(=\sigma_2\sqrt{\frac{a}{\nu_{\mathrm{f}}}}\right)$ is the secondary velocity slip factor, $\alpha_3\left(=\sigma_3\sqrt{\frac{a}{\nu_{\mathrm{f}}}}\right)$ is the thermal slip factor, and $\alpha_4\left(=\sigma_4\sqrt{\frac{a}{\nu_{\mathrm{f}}}}\right)$ is the mass slip factor.

The engineering quantities are demarcated as follows:

$$\text{Skin friction along } x\text{-axis}\left\{C_{\mathrm{fx}} = \frac{\tau_{\mathrm{wx}}}{\rho_{\mathrm{f}}u_{\mathrm{w}}^2}, \right. \tag{20}$$

$$\text{Skin friction along } y\text{-axis}\left\{C_{\mathrm{fy}} = \frac{\tau_{\mathrm{wy}}}{\rho_{\mathrm{f}}v_{\mathrm{w}}^2}, \right. \tag{21}$$

$$\text{Nusselt number}\left\{\mathrm{Nu}_x = \frac{xq_{\mathrm{w}}}{k_{\mathrm{f}}(T_{\mathrm{w}} - T_\infty)}, \right. \tag{22}$$

$$\text{Sherwood number}\left\{\mathrm{Sh}_x = \frac{xq_{\mathrm{m}}}{D_{\mathrm{B}}(C_{\mathrm{w}} - C_\infty)}, \right. \tag{23}$$

where

$$\tau_{\mathrm{w}x} = \mu_{\mathrm{hnf}}\left.\frac{\partial u}{\partial z}\right|_{z=0}, \tag{24}$$

$$\tau_{\mathrm{w}y} = \mu_{\mathrm{hnf}}\left.\frac{\partial v}{\partial z}\right|_{z=0}, \tag{25}$$

$$q_{\mathrm{w}} = -k_{\mathrm{hnf}}\left.\frac{\partial T}{\partial z}\right|_{z=0} + q_{\mathrm{r}}|_{z=0}, \tag{26}$$

$$q_{\mathrm{m}} = -D_{\mathrm{B}}\left.\frac{\partial C}{\partial z}\right|_{z=0}. \tag{27}$$

Thus, we have

$$\text{Skin friction along } x\text{-direction}\left\{\sqrt{\mathrm{Re}_x}\,C_{\mathrm{fx}} = \frac{\mu_{\mathrm{hnf}}}{\mu_{\mathrm{f}}}f''(0), \right. \tag{28}$$

$$\text{Skin friction along } y\text{-direction}\left\{\sqrt{\mathrm{Re}_x}\,C_{\mathrm{fy}} = \frac{\mu_{\mathrm{hnf}}}{\mu_{\mathrm{f}}}g''(0). \right. \tag{29}$$

$$\text{Nusselt number}\left\{\frac{1}{\sqrt{\mathrm{Re}_x}}\mathrm{Nu}_x = -\left(\frac{k_{\mathrm{hnf}}}{k_{\mathrm{f}}} + \mathrm{Rd}\right)\theta'(0), \right. \tag{30}$$

$$\text{Sherwood number}\left\{\frac{1}{\sqrt{\mathrm{Re}_x}}\mathrm{Sh}_x = -\varphi'(0). \right. \tag{31}$$

Here $\mathrm{Re}_x = \frac{xu_{\mathrm{w}}(x)}{\nu_{\mathrm{f}}}$ and $\mathrm{Re}_y = \frac{yv_{\mathrm{w}}(y)}{\nu_{\mathrm{f}}}$ are local Reynolds number.

3 HAM solution

The initial guesses are mathematically designated as follows:

$$\left.\begin{aligned} f_0(\zeta) &= \frac{1}{1+\alpha_1}(1-\mathrm{e}^{-\zeta}),\ g_0(\zeta) = \frac{\delta}{1+\alpha_2}(1-\mathrm{e}^{-\zeta}),\\ \theta_0(\zeta) &= \frac{1}{1+\alpha_3}(1-\mathrm{e}^{-\zeta}),\ \varphi_0(\zeta) = \frac{1}{1+\alpha_4}(-\mathrm{e}^{-\zeta}), \end{aligned}\right\} \tag{32}$$

$$\left.\begin{aligned} L_f(\zeta) &= f''' - f',\ L_g(\zeta) = g''' - g',\\ L_\theta(\zeta) &= \theta'' - \theta,\ L_\varphi(\zeta) = \varphi'' - \varphi, \end{aligned}\right\}, \tag{33}$$

with properties

$$\left.\begin{aligned} L_f(\chi_1 + \chi_2 e^{-\zeta} + \chi_3 e^{\zeta}) &= 0,\ L_g(\chi_4 + \chi_5 e^{-\zeta} + \chi_6 e^{\zeta}) = 0,\\ L_\theta(\chi_7 e^{-\zeta} + \chi_8 e^{\zeta}) &= 0,\ L_\varphi(\chi_9 e^{-\zeta} + \chi_{10} e^{\zeta}) = 0, \end{aligned}\right\}. \tag{34}$$

where $\chi_1 - \chi_{10}$ are constants of general solution.

Moreover,

$$(1-\psi)\,L_f[f(\zeta;\psi) - f_0(\zeta)] = \psi\hbar_f N_f[f(\zeta;\psi), g(\zeta;\psi)], \tag{35}$$

$$(1-\psi)L_g[g(\zeta;\psi) - g_0(\zeta)] = \psi\hbar_g N_g[g(\zeta;\psi), f(\zeta;\psi)], \tag{36}$$

$$\begin{aligned} &(1-\psi)L_\theta[\theta(\zeta;\psi) - \theta_0(\zeta)]\\ &\quad = \psi\hbar_\theta N_\theta[\theta(\zeta;\psi), f(\zeta;\psi), g(\zeta;\psi), \varphi(\zeta;\psi)], \end{aligned} \tag{37}$$

$$\begin{aligned} &(1-\psi)L_\varphi[\varphi(\zeta;\psi) - \varphi_0(\zeta)]\\ &\quad = \psi\ \hbar_\varphi N_\varphi[\varphi(\zeta;\psi), f(\zeta;\psi), g(\zeta;\psi), \theta(\zeta;\psi)], \end{aligned} \tag{38}$$

$$\left.\begin{aligned} &f(0;\psi) = 0, f'(0;\psi) = 1 + \alpha_1 f''(0;\psi),\\ &g'(0;\psi) = \delta + \alpha_2 g''(0;\psi),\\ &g(0;\psi) = 0,\ \theta(0;\psi) = 1 + a_3\theta'(0;\psi),\\ &\varphi(0;\psi) = 1 + a_4\varphi'(0;\psi),\\ &f'(\infty;\psi) = 0, g'(\infty;\psi) = 0,\ \theta(\infty;\psi) = 0,\ \varphi(\infty;\psi) = 0. \end{aligned}\right\} \tag{39}$$

$$\begin{aligned} N_f[f(\zeta;\psi), g(\zeta;\psi)] &= \left(\frac{\mu_{\mathrm{hnf}}/\mu_{\mathrm{f}}}{\mu_{\mathrm{hnf}}/\mu_{\mathrm{f}}}\right)\frac{\partial^3 f(\zeta;\psi)}{\partial\zeta^3}\\ &\quad + (f(\zeta;\psi) + g(\zeta;\psi))\frac{\partial^2 f(\zeta;\psi)}{\partial\zeta^2}\\ &\quad + \left(\frac{\partial f(\zeta;\psi)}{\partial\zeta}\right)^2\\ &\quad - M\left(\frac{\sigma_{\mathrm{hnf}}/\sigma_{\mathrm{f}}}{\mu_{\mathrm{hnf}}/\mu_{\mathrm{f}}}\right)\frac{\partial f(\zeta;\psi)}{\partial\zeta}\\ &\quad - \left(\frac{\mu_{\mathrm{hnf}}/\mu_{\mathrm{f}}}{\mu_{\mathrm{hnf}}/\mu_{\mathrm{f}}}\right)K\frac{\partial f(\zeta;\psi)}{\partial\zeta} = 0, \end{aligned} \tag{40}$$

$$\begin{aligned} &N_g[g(\zeta;\psi), f(\zeta;\psi)]\\ &\quad = \left(\frac{\mu_{\mathrm{hnf}}/\mu_{\mathrm{f}}}{\mu_{\mathrm{hnf}}/\mu_{\mathrm{f}}}\right)\frac{\partial^3 g(\zeta;\psi)}{\partial\zeta^3}\\ &\quad + (g(\zeta;\psi) + f(\zeta;\psi))\frac{\partial^2 g(\zeta;\psi)}{\partial\zeta^2}\\ &\quad + \left(\frac{\partial g(\zeta;\psi)}{\partial\zeta}\right)^2 - \left(\frac{\sigma_{\mathrm{hnf}}/\sigma_{\mathrm{f}}}{\mu_{\mathrm{hnf}}/\mu_{\mathrm{f}}}\right)M\frac{\partial g(\zeta;\psi)}{\partial\zeta}\\ &\quad - \left(\frac{\mu_{\mathrm{hnf}}/\mu_{\mathrm{f}}}{\mu_{\mathrm{hnf}}/\mu_{\mathrm{f}}}\right)K\frac{\partial g(\zeta;\psi)}{\partial\zeta} = 0, \end{aligned} \tag{41}$$

$$\begin{aligned} &N_\theta[\theta(\zeta;\psi), f(\zeta;\psi), g(\zeta;\psi), \varphi(\zeta;\psi)]\\ &\quad = \left(\frac{k_{\mathrm{hnf}}/k_{\mathrm{f}}}{(\rho C_{\mathrm{p}})_{\mathrm{hnf}}/(\rho C_{\mathrm{p}})_{\mathrm{f}}} + \frac{\mathrm{Rd}}{(\rho C_{\mathrm{p}})_{\mathrm{hnf}}/(\rho C_{\mathrm{p}})\mu_{\mathrm{f}}}\right)\frac{\partial^2\theta(\zeta;\psi)}{\partial\zeta^2}\\ &\quad + \mathrm{Pr}(f(\zeta;\psi) + g(\zeta;\psi))\frac{\partial\theta(\zeta;\psi)}{\partial\zeta}\\ &\quad + \mathrm{PrEc}\left(\frac{\mu_{\mathrm{hnf}}/\mu_{\mathrm{f}}}{(\rho C_{\mathrm{p}})_{\mathrm{hnf}}/(\rho C_{\mathrm{p}})_{\mathrm{f}}}\right)\left(\left(\frac{\partial^2 f(\zeta;\psi)}{\partial\zeta^2}\right)^2 + \left(\frac{\partial^2 g(\zeta;\psi)}{\partial\zeta^2}\right)^2\right)\\ &\quad + \frac{Q}{(\rho C_{\mathrm{p}})_{\mathrm{hnf}}/(\rho C_{\mathrm{p}})_{\mathrm{f}}}\theta(\zeta;\psi) + \frac{\mathrm{Pr}}{(\rho C_{\mathrm{p}})_{\mathrm{hnf}}/(\rho C_{\mathrm{p}})_{\mathrm{f}}}\\ &\quad \times\left(\mathrm{Nb}\frac{\partial\theta(\zeta;\psi)}{\partial\zeta}\frac{\partial\varphi(\zeta;\psi)}{\partial\zeta} + \mathrm{Nt}\left(\frac{\partial\theta(\zeta;\psi)}{\partial\zeta}\right)^2\right) = 0, \end{aligned} \tag{42}$$

$$\begin{aligned} &N_\varphi[\varphi(\zeta;\psi), f(\zeta;\psi), g(\zeta;\psi), \theta(\zeta;\psi)]\\ &\quad = \frac{\partial^2\varphi(\zeta;\psi)}{\partial\zeta^2} + \mathrm{Sc}\begin{pmatrix} f(\zeta;\psi)\\ +g(\zeta;\psi)\end{pmatrix}\frac{\partial\varphi(\zeta;\psi)}{\partial\zeta} + \frac{\mathrm{Nt}}{\mathrm{Nb}}\frac{\partial^2\theta(\zeta;\psi)}{\partial\zeta^2}\\ &\quad - \mathrm{Sc}K_{\mathrm{r}}(1+\beta\theta(\zeta;\psi))^n\exp\left(\frac{-E}{1+\beta\theta(\zeta;\psi)}\right)\varphi(\zeta;\psi) = 0. \end{aligned} \tag{43}$$

For $\psi = 0$ and $\psi = 1$, we have

$$\left.\begin{aligned} &f(\zeta;0) = f_0(\zeta),\ f(\zeta;1) = f(\zeta).\\ &g(\zeta;0) = g_0(\zeta),\ g(\zeta;1) = g(\zeta).\\ &\theta(\zeta;0) = \theta_0(\zeta),\ \theta(\zeta;1) = \theta(\zeta).\\ &\varphi(\zeta;0) = \varphi_0(\zeta),\ \varphi(\zeta;1) = \varphi(\zeta). \end{aligned}\right\} \tag{44}$$

By using the Taylor series expansion, we obtain

$$\left.\begin{aligned} f(\zeta;\psi) &= f_0(\zeta) + \sum_{m=1}^{\infty} f_m(\zeta)\psi^m;\\ f_m(\zeta) &= \frac{1}{m!}\frac{\partial^m f(\zeta;\psi)}{\partial\zeta^m}\bigg|_{\psi=0}.\\ g(\zeta;\psi) &= g_0(\zeta) + \sum_{m=1}^{\infty} g_m(\zeta)\psi^m;\\ g_m(\zeta) &= \frac{1}{m!}\frac{\partial^m g(\zeta;\psi)}{\partial\zeta^m}\bigg|_{\psi=0}.\\ \theta(\zeta;\psi) &= \theta_0(\zeta) + \sum_{m=1}^{\infty} \theta_m(\zeta)\psi^m;\\ \theta_m(\zeta) &= \frac{1}{m!}\frac{\partial^m\theta(\zeta;\psi)}{\partial\zeta^m}\bigg|_{\psi=0}.\\ \varphi(\zeta;\psi) &= \varphi_0(\zeta) + \sum_{m=1}^{\infty} \varphi_m(\zeta)\psi^m;\\ \varphi_m(\zeta) &= \frac{1}{m!}\frac{\partial^m\varphi(\zeta;\psi)}{\partial\zeta^m}\bigg|_{\psi=0}. \end{aligned}\right\} \tag{45}$$

The mth-order deformation problem is defined as:

$$\left.\begin{aligned} L_f[f_m(\zeta) - p_m f_{m-1}(\zeta)] &= \hbar_f R_m^f(\zeta),\\ L_g[g_m(\zeta) - p_m g_{m-1}(\zeta)] &= \hbar_g R_m^g(\zeta),\\ L_\theta[\theta_m(\zeta) - p_m\theta_{m-1}(\zeta)] &= \hbar_\theta R_m^\theta(\zeta),\\ L_\varphi[\varphi_m(\zeta) - p_m\varphi_{m-1}(\zeta)] &= \hbar_\varphi R_m^\varphi(\zeta), \end{aligned}\right\} \tag{46}$$

$$\left.\begin{aligned} &f_m(0) = 0, f'_m(0) = 1 + \alpha_1 f''_m(0),\\ &g'_m(0) = \delta + \alpha_2 g''_m(0),\\ &g_m(0) = 0, \theta_m(0) = 1 + \alpha_3 \theta'_m(0),\\ &\varphi_m(0) = 1 + \alpha_4 \varphi'_m(0),\\ &f'_m(\infty) = 0, g'_m(\infty) = 0, \theta_m(\infty) = 0, \varphi_m(\infty) = 0. \end{aligned}\right\}, \quad (47)$$

$$\begin{aligned} R_m^f(\zeta) = {} & \left(\frac{\mu_{\text{hnf}}/\mu_{\text{f}}}{\rho_{\text{hnf}}/\rho_{\text{f}}}\right) f'''_m(\zeta) + \sum_{n=1}^{m-1} f_{m-1-n}(\zeta) f''_n(\zeta)\\ & + \sum_{n=1}^{m-1} g_{m-1-n}(\zeta) f'_n(\zeta) + \sum_{n=1}^{m-1} f'_{m-1-n}(\zeta) f'_n(\zeta)\\ & - M\left(\frac{\sigma_{\text{hnf}}/\sigma_{\text{f}}}{\rho_{\text{hnf}}/\rho_{\text{f}}}\right) f'_m(\zeta) - \left(\frac{\mu_{\text{hnf}}/\mu_{\text{f}}}{\rho_{\text{hnf}}/\rho_{\text{f}}}\right) K f'_m(\zeta), \end{aligned} \quad (48)$$

$$\begin{aligned} R_m^g(\zeta) = {} & \left(\frac{\mu_{\text{hnf}}/\mu_{\text{f}}}{\rho_{\text{hnf}}/\rho_{\text{f}}}\right) g'''_m(\zeta) + \sum_{n=1}^{m-1} g_{m-1-n}(\zeta) g'_n(\zeta)\\ & + \sum_{n=1}^{m-1} f_{m-1-n}(\zeta) g'_n(\zeta) + \sum_{n=1}^{m-1} g'_{m-1-n}(\zeta) g'_n(\zeta)\\ & - M\left(\frac{\sigma_{\text{hnf}}/\sigma_{\text{f}}}{\rho_{\text{hnf}}/\rho_{\text{f}}}\right) g'_m(\zeta) - \left(\frac{\mu_{\text{hnf}}/\mu_{\text{f}}}{\rho_{\text{hnf}}/\rho_{\text{f}}}\right) K g'_m(\zeta), \end{aligned} \quad (49)$$

$$\begin{aligned} R_m^\theta(\zeta) = {} & \left(\frac{k_{\text{hnf}}/k_{\text{f}}}{(\rho C_{\text{p}})_{\text{hnf}}/(\rho C_{\text{p}})_{\text{f}}} + \frac{\text{Rd}}{(\rho C_{\text{p}})_{\text{hnf}}/(\rho C_{\text{p}})\mu_{\text{f}}}\right) \theta''_m(\zeta)\\ & + \text{Pr}\left(\sum_{n=1}^{m-1} f_{m-1-n}(\zeta)\theta'_n(\zeta) + \sum_{n=1}^{m-1} g_{m-1-n}(\zeta)\theta'_n(\zeta)\right)\\ & + \frac{\text{Pr}Q}{(\rho C_{\text{p}})_{\text{hnf}}/(\rho C_{\text{p}})_{\text{f}}}\theta_m(\zeta)\\ & + \text{PrEc}\left(\frac{\mu_{\text{hnf}}/\mu_{\text{f}}}{(\rho C_{\text{p}})_{\text{hnf}}/(\rho C_{\text{p}})_{\text{f}}}\right)\\ & \left(\sum_{n=1}^{m-1} f''_{m-1-n}(\zeta) f''_n(\zeta) + \sum_{n=1}^{m-1} g''_{m-1-n}(\zeta) g''_n(\zeta)\right)\\ & + \frac{\text{Pr}}{(\rho C_{\text{p}})_{\text{hnf}}/(\rho C_{\text{p}})_{\text{f}}}\left(\text{Nb}\sum_{n=1}^{m-1}\theta'_{m-1-n}(\zeta)\varphi'_n(\zeta)\right.\\ & \left. + \text{Nt}\sum_{n=1}^{m-1}\theta'_{m-1-n}(\zeta)\theta'_n(\zeta)\right), \end{aligned} \quad (50)$$

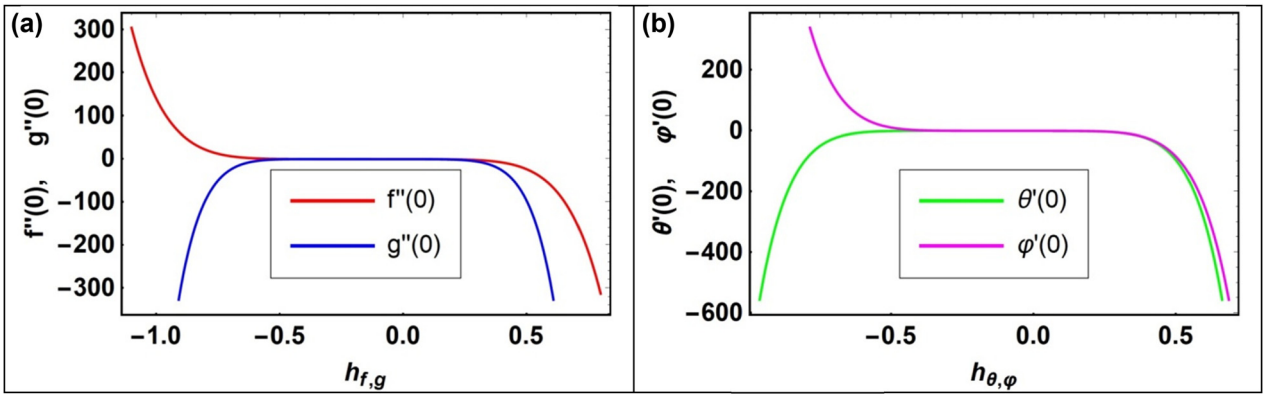

Figure 2: (a) $\hbar$ curves for $f''(0)$ and $g''(0)$. (b) $\hbar$ curves for $\theta'(0)$ and $\varphi'(0)$.

$$R_m^{\varphi}(\zeta) = \varphi''_m(\zeta) + \mathrm{Sc}\left\{\sum_{n=1}^{m-1} f_{m-1-n}(\zeta)\varphi'_n(\zeta) + \sum_{n=1}^{m-1} g_{m-1-n}(\zeta)\theta'_n(\zeta)\right\} + \frac{\mathrm{Nt}}{\mathrm{Nb}}\theta''_m(\zeta) - \mathrm{Sc}K_r(1+\beta\theta_m(\zeta))^n \exp\left(\frac{-E}{1+\beta\theta_m(\zeta)}\right)\varphi_m(\zeta), \quad (51)$$

where

$$p_m = \begin{cases} 0, & m \le 1 \\ 1, & m > 1 \end{cases}. \quad (52)$$

4 Convergence of HAM

Figure 2(a) and (b) depicts the convergence areas of different flow profiles of the modeled equations. HAM is a powerful method which can solve both linear and nonlinear differential equations. Also, HAM ensures the convergence area of the flow problem which validates the correctness of method. For the modeled equations, the convergence areas of the velocities, thermal and concentration panels are depicted in Figure 2(a) and (b). The convergence areas of the x-direction velocity is $-0.8 \le \hbar_f \le 0.5$, y-direction velocity is $-0.6 \le \hbar_g \le 0.35$, temperature is $-0.6 \le \hbar_\theta \le 0.4$, and concentration is $-0.5 \le \hbar_\varphi \le 0.4$.

5 Analysis and discussion of results

This paragraph shows the results and discussion of the present model. The flow fluid is considered on a stretching sheet. Figures 3–20 are displayed to see the influence effects of various factors on diverse flow distributions. The values of various factors are selected as $\phi_1 = \phi_2 = 0.04$, $M = 0.5$, $\mathrm{Pr} = 6.2$, $\mathrm{Ec} = 0.1$, $K_r = 0.5$, $Q = 1.0$, $\mathrm{Nt} = 0.1$, $\mathrm{Nb} = 0.1$, $\mathrm{Sc} = 1.0$, $\beta = 1.1$, $E = 0.3$, $K = 0.2$, $\alpha_1 = \alpha_2 = \alpha_3 = \alpha_4 = 0.5$, and $\delta = 0.2$.

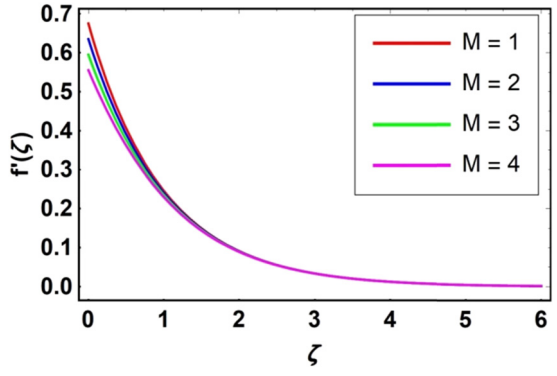

Figure 3: Variation in velocity profile $f'(\zeta)$ *via* magnetic factor M.

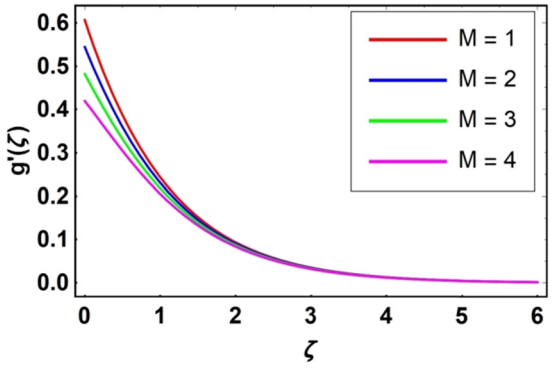

Figure 4: Variation in velocity profile $g'(\zeta)$ *via* magnetic factor M.

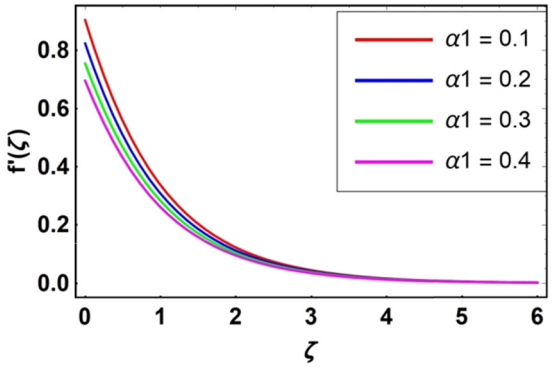

Figure 5: Variation in velocity profile $f'(\zeta)$ *via* primary velocity slip factor α_1.

5.1 Analysis of results

5.1.1 Discussion of results

Figures 3 and 4 demonstrate the impression of M on velocities $f'(\zeta)$ and $g'(\zeta)$. Both profiles are reducing functions of magnetic factor. Actually, the increase in M generates Lorentz force which counterattacks the fluid's motion. This opposing force is due to the higher skin friction at sheet's

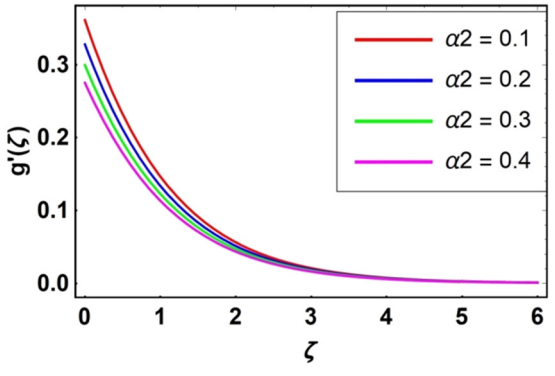

Figure 6: Variation in velocity profile $g'(\zeta)$ *via* secondary velocity slip factor α_2.

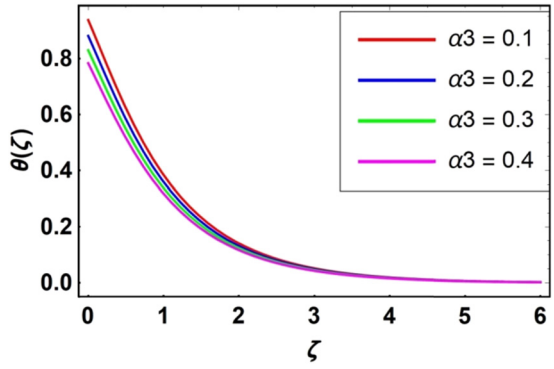

Figure 7: Impact of variation in temperature profile $\theta(\zeta)$ *via* thermal slip factor α_3.

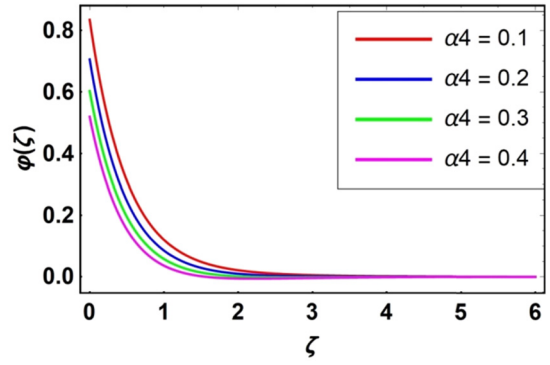

Figure 8: Variation in concentration profile $\varphi(\zeta)$ *via* concentration slip factor α_4.

surface. Therefore, the higher magnetic factor lessens the velocities in all directions. So, both $f'(\zeta)$ and $g'(\zeta)$ are the reducing functions of M. The results of the primary velocity slip factor α_1 and the secondary velocity slip factor α_2 on both $f'(\zeta)$ and $g'(\zeta)$ are described in Figures 5 and 6. It is detected that both $f'(\zeta)$ and $g'(\zeta)$ escalate with the increase in the primary velocity slip factor α_1 and the

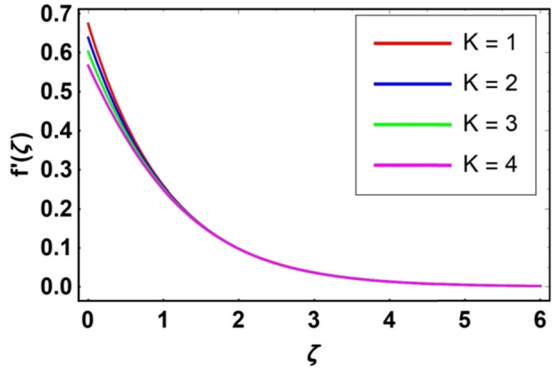

Figure 9: Variation in velocity profile $f'(\zeta)$ *via* porosity factor K.

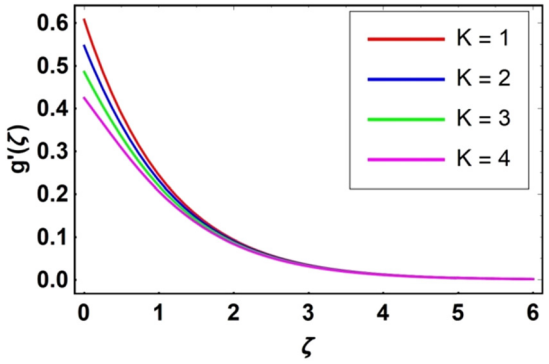

Figure 10: Variation in velocity profile $g'(\zeta)$ *via* porosity factor K.

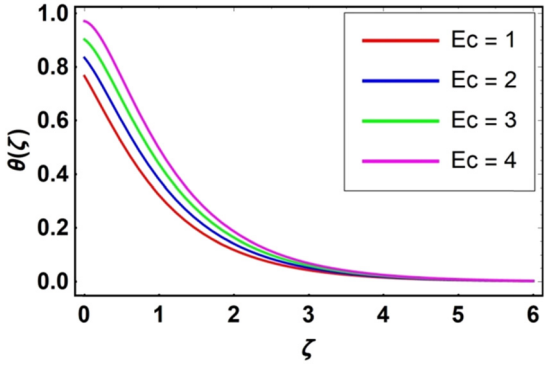

Figure 11: Variation in temperature profile $\theta(\zeta)$ *via* Eckert number Ec.

secondary velocity slip factor α_2. Figures 7 and 8 explain the outcomes of the thermal slip factor σ_3 and mass slip factor α_4, respectively, on $\theta(\zeta)$ and $\varphi(\zeta)$. It is observed that under the increment of thermal slip factor σ_3 and mass slip factor α_4, both temperature profile and concentration profile have decreased, respectively. Figures 9 and 10 describe the fluctuation of $f'(\zeta)$ and $g'(\zeta)$ for the increase in the porosity parameter K. Figures 9 and 10 specify that $f'(\zeta)$

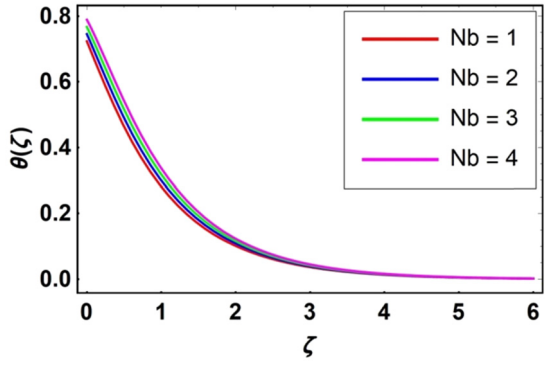

Figure 12: Variation in temperature profile $\theta(\zeta)$ *via* Brownian motion factor Nb.

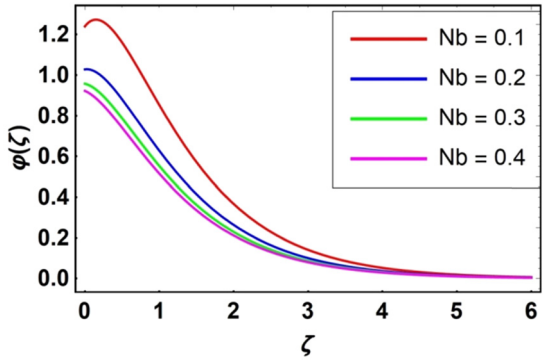

Figure 13: Variation in concentration $\varphi(\zeta)$ *via* Brownian motion factor Nb.

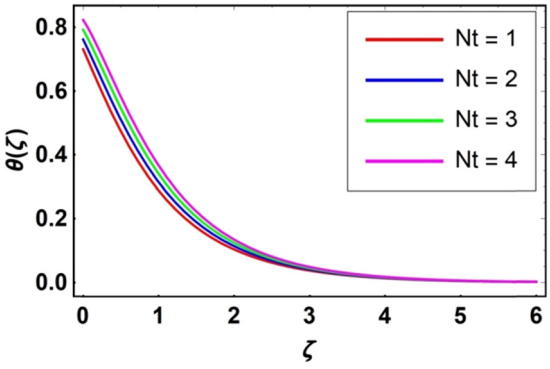

Figure 14: Variation in temperature profile $\theta(\zeta)$ *via* thermophoresis factor Nt.

and $g'(\zeta)$ reduces due to the increase in the porosity parameter K. The relationship between Ec and $\theta(\zeta)$ is exposed in Figure 11. It is shown in this figure that $\theta(\zeta)$ is observed for increase in Ec. An increase in Eckert number amplifies the kinetic energy of the nanofluid, which is directly proportional to the temperature, leading to an elevation in the thermal properties of the nanofluid. Physically, an increase

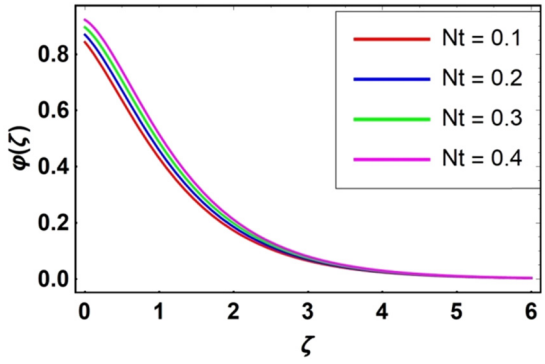

Figure 15: Variation in concentration profile $\varphi(\zeta)$ *via* thermophoresis factor Nt.

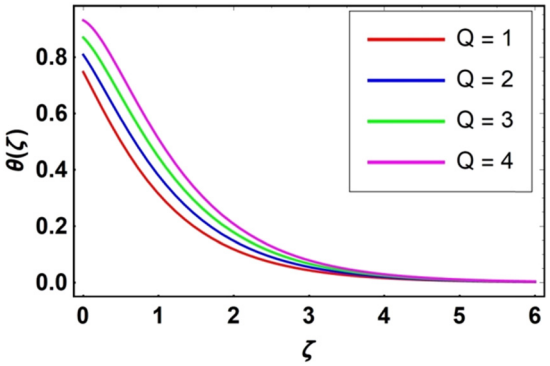

Figure 16: Variation in temperature profile $\theta(\zeta)$ *via* heat source factor Q.

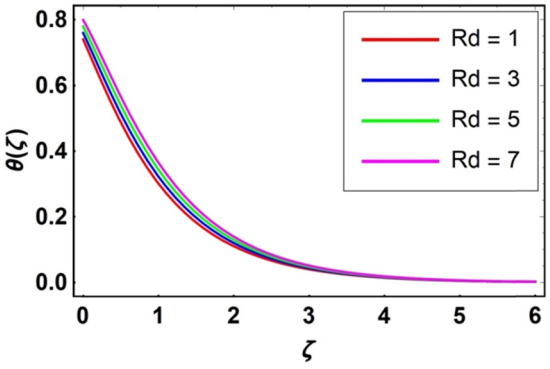

Figure 17: Variation in temperature profile $\theta(\zeta)$ *via* thermal radiation factor Rd.

in Ec causes conversion of mechanical to thermal energy that leads to an escalation in thermal distribution. In Figure 12, the magnitude of $\theta(\zeta)$ against greater values of Nb is discussed. It describes that with the increase in Brownian motion parameter Nb, hybrid nanofluid temperature profile $\theta(\zeta)$ intensifies. Additionally, the random movement of molecules increases the kinetic energy of the system, leading to a strengthening of the thermal

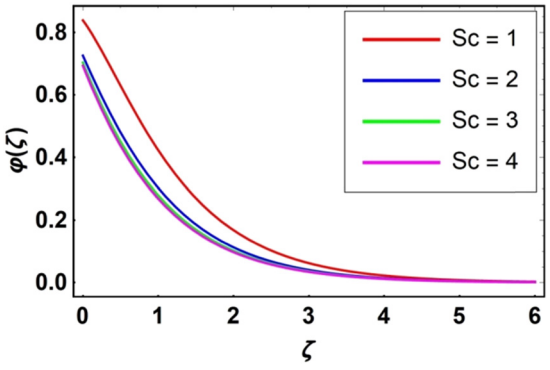

Figure 18: Variation in concentration profile $\varphi(\zeta)$ *via* Schmidt number Sc.

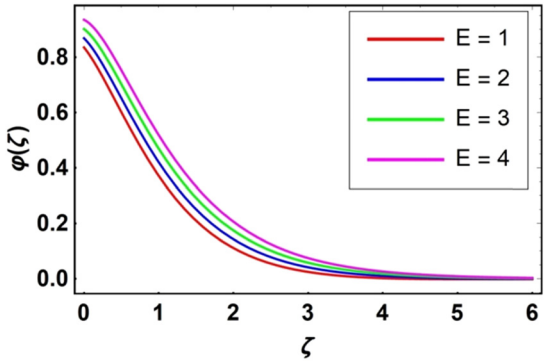

Figure 19: Variation in concentration profile $\varphi(\zeta)$ *via* activation energy factor E.

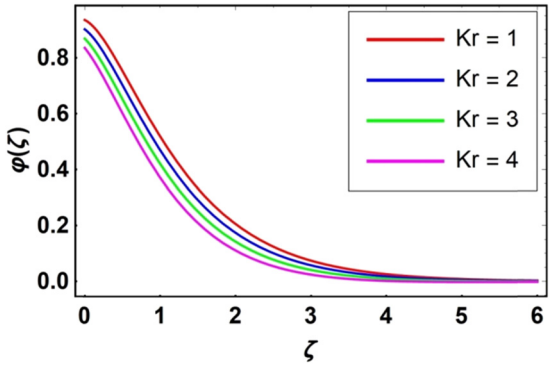

Figure 20: Variation in concentration profile $\varphi(\zeta)$ *via* chemical reaction factor Kr.

distribution. The variation in Nb on the concentration profile $\varphi(\zeta)$ is presented in Figure 13. The increase in Nb leads to the reduction in the hybrid nanofluid concentration distribution $\varphi(\zeta)$. In physical point of view, the solutal distribution diminishes when the mass diffusion coefficient decreases and viscosity deteriorates with an increase in Nb. The alteration in $\theta(\zeta)$ of fluid with respect to the increase in Nt is described in Figure 14. The temperature

Table 2: Comparison of current data for $-g''(0)$ with work of Ramzan *et al.* [47]

δ	$-g''(0)$	
	Ramzan *et al.* [47]	**Present results**
0.0	0.0	0.0000000
0.1	0.073015	0.0730169
0.2	0.158223	0.1582240
0.3	0.254345	0.2543469
0.4	0.360590	0.3605902
0.5	0.476291	0.4762920

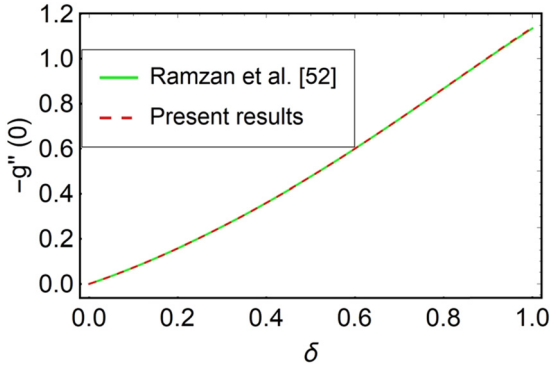

Figure 21: Comparison of current data for $-g''$ (0) with work of Ramzan *et al.* [47].

Table 3: Impacts of M and K on $\frac{\mu_{\text{hnf}}}{\mu_{\text{f}}}f''(0)$ and $\frac{\mu_{\text{hnf}}}{\mu_{\text{f}}}g''(0)$

M	K	$\frac{\mu_{\text{hnf}}}{\mu_{\text{f}}}f''(0)$	$\frac{\mu_{\text{hnf}}}{\mu_{\text{f}}}g''(0)$
0.4		1.578645	1.280633
0.6		1.653848	1.306885
0.8		1.726806	1.325946
	0.1	0.480742	0.478532
	0.2	0.508967	0.480652
	0.3	0.525809	0.497963

profile is amplifying for increase in thermophoresis factor Nt. Influence of thermophoresis factor Nt on the concentration profile $\varphi(\zeta)$ of fluid is displayed in Figure 15. For greater values of Nt, the value of $\varphi(\zeta)$ is lower. The features of the heat generation factor Q on $\theta(\zeta)$ of hybrid nanofluid are examined in Figure 18. It is found that an increase in Q

Table 4: Impacts of different factors on $-\left(\frac{k_{\text{hnf}}}{k_{\text{f}}} + \text{Rd}\right)\theta'(0)$

Rd	Ec	Nb	Nt	Q	$-\left(\frac{k_{\text{hnf}}}{k_{\text{f}}}+\text{Rd}\right)\theta'(0)$
0.1					1.568757
0.2					1.608754
0.3					1.636709
	0.1				1.113578
	0.2				1.909757
	0.3				1.287537
		0.1			1.579986
		0.2			1.608864
		0.3			1.640875
			0.1		1.808646
			0.2		1.824575
			0.3		1.846906
				0.1	1.253689
				0.2	1.298764
				0.3	1.357896

increased the hybrid nanofluid thermal distribution. The physical reason for increase in $\theta(\zeta)$ is the increase in Q, which produces more energy. This justifies that temperature is higher for the greater values of Q. The fluctuation in hybrid nanofluid temperature profile $\theta(\zeta)$ due to an increase in Rd is deliberated in Figure 17. Higher values of Rd amplified $\theta(\zeta)$. Actually, the thermal radiation is the measurement of the electromagnetic radiation emitted by a fluid element. This radiation is then transformed into thermal radiation that increases $\theta(\zeta)$. Influence of Sc on $\varphi(\zeta)$ is visualized in Figure 18. It is detected that $\varphi(\zeta)$ decreases due to an increase in Sc. Actually, Sc relates momentum diffusion to mass diffusion of fluid. When Sc increases, it indicates that the mass diffusivity is decreasing relative to momentum diffusivity; therefore, increase in Sc leads to a weakening in $\varphi(\zeta)$ due to the reduced mass diffusivity of the nanoparticles. The impression of activation energy factor E on the hybrid nanofluid concentration distribution $\varphi(\zeta)$ is explained in Figure 19. Increasing estimates of E amplifies $\varphi(\zeta)$ of the hybrid nanofluid. As E increases, the modified Arrhenius function diminishes in a physical sense. Therefore, the hybrid nanofluid concentration profile $\varphi(\zeta)$ shows an increasing role for the increase in E. Figure 20 displays the impacts of Kr on $\varphi(\zeta)$. The declining role of $\varphi(\zeta)$ is examined for increase in Kr. In Table 2 and Figure 21, the current data are compared with that of Ramzan *et al.* [47]. The present results of the existing work show fine promise with the published data. Table 3 depicts the variation in skin friction coefficient $\frac{\mu_{\text{hnf}}}{\mu_{\text{f}}} f''(0)$ in x-direction, and skin friction coefficient $\frac{\mu_{\text{hnf}}}{\mu_{\text{f}}} g''(0)$ in y-direction for an increase in M, and porosity factor K. Both $\frac{\mu_{\text{hnf}}}{\mu_{\text{f}}} f''(0)$ and $\frac{\mu_{\text{hnf}}}{\mu_{\text{f}}} g''(0)$ are amplified for increasing values of M and K. Similarly, the physical aspects of radiation parameter Rd, Eckert number Ec, Brownian factor Nb, and thermophoresis factor Nt on the heat transport rate are deliberated in Table 4. It is found that the Improvement in radiation parameter Rd, Ec, Nb, and Nt led to improve the heat transport rate mechanism.

6 Conclusion

The present problem determines the heat and mass transport characteristics across the stretching surface through the porous media. The velocity, thermal and concentration slip conditions are adopted in this analysis. HAM technique is employed for the simulation of highly nonlinear ODEs. In graphical form, the computation of how various physical parameters impact diverse flow profiles is presented. In this work, the significant key findings are examined and discussed, which include

- The primary velocity profile declines due to magnetic field parameter, primary slip parameter, and porosity parameter.
- Increment in magnetic field parameter, secondary velocity slip parameter, and porosity parameter led to amplifying the secondary velocity profile.
- Thermal profile is weakened for upsurge in thermal slip factor but amplification in Eckert number, Brownian factor, heat generation factor, and thermal radiation factor amplified the thermal profile.
- It is examined that the concentration distribution is greater for thermophoresis factor, and activation energy parameter. Further, reduction in concentration profile is observed for a solutal slip, Brownian, chemical reaction factors, and Schmidt number.
- Heat transport rate shows increment behavior due to the increment in radiation parameter, Eckert number, Brownian motion, and thermophoresis factors.
- With the enhancement of magnetic and porosity factors, the coefficients of skin friction in both x- and y-directions are amplified.
- Further comparison of the existing work is also discussed and shows good agreements with the published results.
- The present model can be modified by taking other types of fluid and coordinate system. Different types of physical effects and methodologies can be used to solve proposed model.
- It has been observed that velocity in x-direction converges in the region $-0.8 \le \hbar_{\text{f}} \le 0.5$, in y-direction velocity is convergent in the zone $-0.6 \le \hbar_{\text{g}} \le 0.35$, while temperature converges in the region $-0.6 \le \hbar_{\theta} \le 0.4$, and concentration converges in the region $-0.5 \le \hbar_{\varphi} \le 0.4$.
- In future, the impacts of variable porous space will be incorporated in the proposed mathematical model to observe its impacts on velocity distribution and thermal transportation for hybrid nanofluid flow.

Funding information: Princess Nourah bint Abdulrahman University Researchers Supporting Project number (PNURSP2024R443), Princess Nourah bint Abdulrahman University, Riyadh, Saudi Arabia. This work was supported by the Deanship of Scientific Research, the Vice Presidency for Graduate Studies and Scientific Research, King Faisal University, Saudi Arabia (Grant No. 6036).

Author contributions: All authors have accepted responsibility for the entire content of this manuscript and approved its submission.

Conflict of interest: The authors state no conflict of interest.

Data availability statement: All data generated or analyzed during this study are included in this published article.

References

[1] Choi SUS, Eastman JA. Enhancing thermal conductivity of fluids with nanoparticles. 1995 Int Mech Eng Congr Exhib San Fr CA (United States), 12–17 Nov 1995 [Internet]; 1995. [cited 2021 Oct 2] https://digital.library.unt.edu/ark:/67531/metadc671104/.

[2] Hashemi SMH, Fazeli SA, Zirakzadeh H, Ashjaee M. Study of heat transfer enhancement in a nanofluid-cooled miniature heat sink. Int Commun Heat Mass Transf. 2012;39:877–84.

[3] Habib D, Salamat N, Abdal S, Siddique I, Salimi M, Ahmadian A. On time dependent MHD nanofluid dynamics due to enlarging sheet with bioconvection and two thermal boundary conditions. Microfluid Nanofluidics. 2022;26:11.

[4] Chu Y, Bashir S, Ramzan M, et al. Model-based comparative study of magnetohydrodynamics unsteady hybrid nanofluid flow between two infinite parallel plates with particle shape effects. Math Methods Appl Sci. 2022.

[5] Eid MR, Nafe MA. Thermal conductivity variation and heat generation effects on magneto-hybrid nanofluid flow in a porous medium with slip condition. Waves Random Complex Media. 2022;32:1103–27.

[6] Rajput VD, Minkina T, Upadhyay SK, Kumari A, Ranjan A, Mandzhieva S, et al. Nanoparticle's radius effect on unsteady mixed convective copper-water nanofluid flow over an expanding sheet in porous medium with boundary slip. Chem Eng J Adv. 2022;12:100366.

[7] Sarfraz M, Khan M. Cattaneo-Christov double diffusion based heat transport analysis for nanofluid flows induced by a moving plate. Numer Heat Transf Part A Appl. 2024;85:351–63.

[8] Dawar A, Wakif A, Thumma T, Shah NA. Towards a new MHD non-homogeneous convective nanofluid flow model for simulating a rotating inclined thin layer of sodium alginate-based iron oxide exposed to incident solar energy. Int Commun Heat Mass Transf. 2022;130:105800.

[9] Pasha AA, Islam N, Jamshed W, Alam MI, Jameel AGA, Juhany KA, et al. Statistical analysis of viscous hybridized nanofluid flowing *via* Galerkin finite element technique. Int Commun Heat Mass Transf. 2022;137:106244.

[10] Ojjela O. Numerical investigation of heat transport in alumina–silica hybrid nanofluid flow with modeling and simulation. Math Comput Simul. 2022;193:100–22.

[11] Sarfraz M, Khan M, Al-Zubaidi A, Saleem S. Tribology-informed analysis of convective energy transfer in ternary hybrid nanofluids on inclined porous surfaces. Tribol Int. 2023;188:108860.

[12] Salahuddin T, Siddique N, Khan M, Chu YM. A hybrid nanofluid flow near a highly magnetized heated wavy cylinder. Alex Eng J. 2022;61:1297–308.

[13] Zhang L, Bhatti MM, Michaelides EE, Marin M, Ellahi R. Hybrid nanofluid flow towards an elastic surface with tantalum and nickel nanoparticles, under the influence of an induced magnetic field. Eur Phys J Spec Top. 2022;231:521–33.

[14] Sarfraz M, Khan M, Al-Zubaidi A, Saleem S. Insights into the thermodynamic efficiency of Homann-Agrawal hybrid nanofluid flow. Alex Eng J. 2023;82:178–85.

[15] Alrabaiah H, Bilal M, Khan MA, Muhammad T, Legas EY. Parametric estimation of gyrotactic microorganism hybrid nanofluid flow between the conical gap of spinning disk-cone apparatus. Sci Rep. 2022;12:1–14.

[16] Ouni M, Ladhar LM, Omri M, Jamshed W, Eid MR. Solar water-pump thermal analysis utilizing copper–gold/engine oil hybrid nanofluid flowing in parabolic trough solar collector: Thermal case study. Case Stud Therm Eng. 2022;30:101756.

[17] Bharathi V, Prakash J, Tripathi D, Anwar Bég O, Ashish S, Ravi S. Heat transfer in EMHD hyperbolic tangent ternary hybrid nanofluid flow over a Darcy-Forchheimer porous wedge surface: A numerical simulation. Nanomater Nanoliquids Appl Energy Environ. Springer; 2023. p. 249–79

[18] Pandey AK, Rajput S, Bhattacharyya K, Sibanda P. Impact of metal oxide nanoparticles on unsteady stagnation point flow of the hybrid base fluid along a flat surface. Pramana. 2021;95:5.

[19] Ahmed F, Akbar NS, Tripathi D. Numerically hydrothermal fully developed forced convective hybrid nanofluid flow through annular sector duct. Mod Phys Lett B. 2024;38:2450029.

[20] Singh SP, Kumar M, Yaseen M, Rawat SK. Insight into influence of thermal radiation and Cattaneo–Christov model on ternary hybrid nanofluid (TiO_2–Al_2O_3–MoS_2/kerosene oil) and hybrid nanofluid (TiO_2–Al_2O_3/kerosene oil) flow and heat transfer over a stretching sheet. Numer Heat Transf Part A Appl. 2023;1–21.

[21] Algehyne EA, Saeed A, Arif M, Bilal M, Kumam P, Galal AM. Gyrotactic microorganism hybrid nanofluid over a Riga plate subject to activation energy and heat source: Numerical approach. Sci Rep. 2023;13:13675.

[22] Raizah Z, Alrabaiah H, Bilal M, Junsawang P, Galal AM. Numerical study of non-Darcy hybrid nanofluid flow with the effect of heat source and Hall current over a slender extending sheet. Sci Rep. 2022;12:16280.

[23] Mishra NK, Anwar S, Kumam P, Seangwattana T, Bilal M, Saeed A. Numerical investigation of chemically reacting jet flow of hybrid nanofluid under the significances of bio-active mixers and chemical reaction. Heliyon. 2023;9:17678.

[24] Dey S, Ghosh S, Mukhopadhyay S. MHD mixed convection chemically reactive nanofluid flow over a vertical plate in presence of slips and zero nanoparticle flux. Waves Random Complex Media. 2023;1–20.

[25] Goud Bejawada S, Dharmendar Reddy Y, Jamshed W, Nisar KS, Alharbi AN, Chouikh R. Radiation effect on MHD Casson fluid flow over an inclined non-linear surface with chemical reaction in a Forchheimer porous medium. Alex Eng J. 2022;61:8207–20.

[26] Vishalakshi AB, Mahabaleshwar US, Sarris IE. An MHD fluid flow over a porous stretching/shrinking sheet with slips and mass transpiration. Micromachines. 2022;13:116.

[27] Upreti H, Rawat SK, Kumar M. Radiation and non-uniform heat sink/source effects on 2D MHD flow of CNTs-H_2O nanofluid over a flat porous plate. Multidiscip Model Mater Struct. 2019;16:791–809.

[28] Sharma K, Kumar S, Narwal A, Mebarek-Oudina F, Animasaun IL. Convective MHD fluid flow over stretchable rotating disks with Dufour and Soret effects. Int J Appl Comput Math. 2022;8:1–12.

[29] Raghunath K, Gulle N, Vaddemani RR, Mopuri O. Unsteady MHD fluid flow past an inclined vertical porous plate in the presence of

chemical reaction with aligned magnetic field, radiation, and Soret effects. Heat Transf. 2022;51:2742–60.
[30] Gautam AK, Rajput S, Bhattacharyya K, Pandey AK, Chamkha AJ, Begum M. Comparative study of two non-Newtonian fluids with bioconvective induced MHD flow in presence of multiple slips, heat source/sink and nonlinear thermal radiation. Chem Eng J Adv. 2022;12:100365.
[31] Maiti H, Mukhopadhyay S. Existence of MHD boundary layer hybrid nanofluid flow through a divergent channel with mass suction and injection. Chem Eng J Adv. 2023;14:100475.
[32] Sarwar N, Jahangir S, Asjad MI, Eldin SM. Application of ternary nanoparticles in the heat transfer of an MHD non-newtonian fluid flow. Micromachines. 2022;13:2149.
[33] Maiti H, Mukhopadhyay S. Flow of viscous fluid over a still nano-fluid in presence of shear. Forces Mech. 2022;9:100148.
[34] Saha D, Mahanta A, Mukhopadhyay S, Sengupta S. Cattaneo–Christov heat and mass flux model for Electromagnetohydrodynamic (EMHD) non-Newtonian flow of Jeffrey nanofluid with nonlinear thermal radiation and stratified boundary conditions. Waves Random Complex Media. 2023;1–25.
[35] Akbar Qureshi Z, Bilal S, Khan U, Akgül A, Sultana M, Botmart T, et al. Mathematical analysis about influence of Lorentz force and interfacial nano layers on nanofluids flow through orthogonal porous surfaces with injection of SWCNTs. Alex Eng J. 2022;61:12925–41.
[36] Verma AK, Rajput S, Bhattacharyya K, Chamkha AJ, Yadav D. Comparison between graphene-water and graphene oxide-water nanofluid flows over exponential shrinking sheet in porous medium: dual solutions and stability analysis. Chem Eng J Adv. 2022;12:100401.
[37] Raza Q, Qureshi MZA, Khan BA, Kadhim Hussein A, Ali B, Shah NA, et al. Insight into Dynamic of Mono and Hybrid Nanofluids Subject to Binary Chemical Reaction, Activation Energy, and Magnetic Field through the Porous Surfaces. Mathematics. 2022;10:10.
[38] Krishna MV, Chamkha AJ. Thermo-diffusion, chemical reaction, Hall and ion slip effects on MHD rotating flow of micro-polar fluid past an infinite vertical porous surface. Int J Ambient Energy. 2022;43:5344–56.
[39] Megahed AM, Abbas W. Non-Newtonian cross fluid flow through a porous medium with regard to the effect of chemical reaction and thermal stratification phenomenon. Case Stud Therm Eng. 2022;29:101715.
[40] Pandey AK, Upreti H, Joshi N, Uddin Z. Effect of natural convection on 3D MHD flow of MoS_2–GO/H_2O *via* porous surface due to multiple slip mechanisms. J Taibah Univ Sci. 2022;16:749–62.
[41] Hayat T, Qayyum S, Imtiaz M, Alsaedi A. Three-dimensional rotating flow of Jeffrey fluid for Cattaneo-Christov heat flux model. AIP Adv. 2016;6:25012.
[42] Raspo I, Hugues S, Serre E, Randriamampianina A, Bontoux P. A spectral projection method for the simulation of complex three-dimensional rotating flows. Comput Fluids. 2002;31:745–67.
[43] Cao W, I.L. A, Yook S-J, V.A. O, Ji X. Simulation of the dynamics of colloidal mixture of water with various nanoparticles at different levels of partial slip: Ternary-hybrid nanofluid. Int Commun Heat Mass Transf. 2022;135:106069.
[44] Song Y-Q, Obideyi BD, Shah NA, Animasaun IL, Mahrous YM, Chung JD. Significance of haphazard motion and thermal migration of alumina and copper nanoparticles across the dynamics of water and ethylene glycol on a convectively heated surface. Case Stud Therm Eng. 2021;26:101050.
[45] Massoudi MD, Ben Hamida MB. MHD natural convection and thermal radiation of diamond–water nanofluid around rotating elliptical baffle inside inclined trapezoidal cavity. Eur Phys J Plus. 2020;135:1–24.
[46] Sen SSS, Das M, Mahato R, Shaw S. Entropy analysis on nonlinear radiative MHD flow of Diamond-Co_3O_4/ethylene glycol hybrid nanofluid with catalytic effects. Int Commun Heat Mass Transf. 2021;129:105704.
[47] Ramzan M, Shaheen N, Ghazwani HAS, Elmasry Y, Kadry S, Mehmood Y. Application of Corcione correlation in a nanofluid flow on a bidirectional stretching surface with Cattaneo–Christov heat flux and heat generation/absorption. Numer Heat Transf Part A Appl. 2022;1–17.